From adsorptation to dissipation: insights from computer simulations of solid H2O and CO

Ferrari, B.C.

Chapter 6

Vibrational Energy Relaxation in Solid Carbon Monoxide

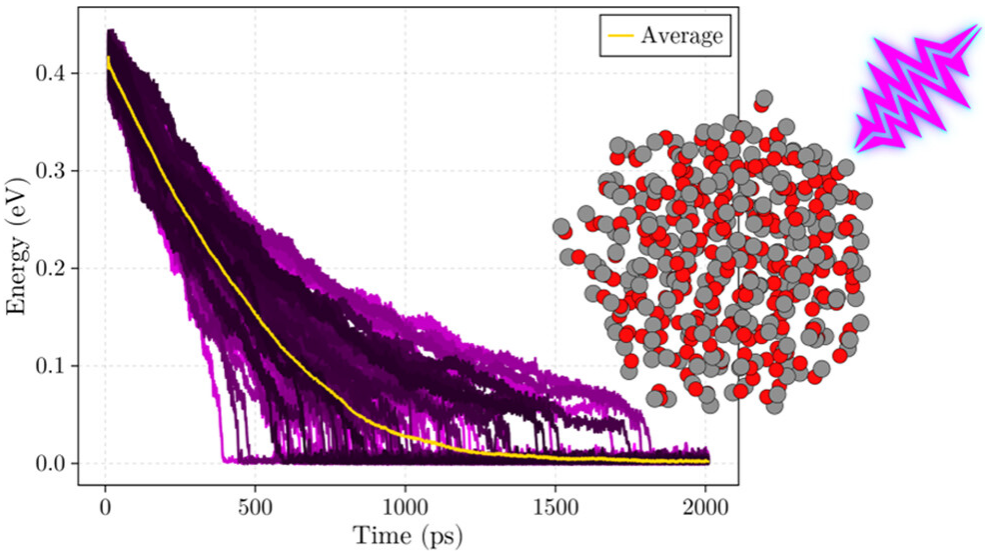

This chapter is based on:
Ferrari, B. C., van Hemert, M., Meyer, J., & Lamberts, T. (2024). Vibrational Energy Relaxation in Solid Carbon Monoxide. The Journal of Physical Chemistry C, 128(49), 21060-21072.

6.1 Abstract

Theory predicts vibrational energy relaxation (VER) in a dense medium exhibits an exponential dependence on the order of the multiphonon process (energy-gap law). Simply put, the vibrational energy decay rate (τ^{-1}) has an exponential dependence on the difference between the excited and accepting frequencies $\Delta\nu$ (frequency-gap law). Additionally, the vibrational density of states (VDOS) of the "bath" of low-frequency modes, into which vibrational energy is being dissipated, play a role in the VER. Although analytical studies at the quantum mechanical level for model systems have provided great insights, quantification of VER dynamics for systems described by realistic interaction potentials are still scarce. Here we focus on a simple diatomic molecule (carbon monoxide) to exclusively probe intermolecular VER without contributions from intramolecular vibrational energy redistribution. Using classical non-equilibrium molecular dynamics (NEMD) simulations we study VER within amorphous and crystalline clusters for mixtures of four different carbon monoxide isotopologues all described by two different interaction potentials. We also present a novel method for extracting $\tau(\Delta\nu)$ for trajectory ensembles of such NEMD simulations of weakly coupled molecules that have slow dissipation rates. For amorphous clusters, $\tau(\Delta\nu)$ is best described by a bi-exponential fit, whereas the situation is more complicated for crystalline clusters. In both cases we find links to the VDOS. Although the energy transfer occurs continuously in our classical simulations, further analysis of our trajectory ensembles suggests very interesting analogies to quantum mechanical descriptions of non-resonant and resonant vibrational to vibrational (V–V) energy transfer.

6.2 Introduction

An essential step in many chemical and physical processes in condensed phase is vibrational energy relaxation (VER).[1] For instance, an intermediate formed via an exothermic step may be vibrationally excited, and the VER rate or pathway may determine the subsequent step in the reaction.[2,3] Furthermore, vibrational energy transfer is essential for understanding energy flow in proteins[4,5], chemical reactions[6], molecular collisions[7,8], and between interfaces[9,10]. As such, an understanding of VER at the atomic scale is very important in physical and theoretical chemistry.

In pursuit of a theoretical framework for vibrational energy transfer, theoreticians initially turned to analogous radiationless transitions, such as, electronic relaxation.

Electronic relaxation has been shown to obey the energy gap law, which states that the transition probability has an exponential dependence on the energy gap between the two electronic states.[11] Nitzan *et al.*[12] derived an analogous expression for VER in a dense medium, where the VER rate exhibits an exponential dependence on the order of the multiphonon process. The order of the multiphonon process is given by the number of phonons that need to be created to accept the vibrational energy. In VER theory the energy-gap is more commonly expressed as a vibrational frequency-gap, as such, within this context its simpler to refer to it as the frequency-gap law.[13] Sun *et al.*[13] studied the vibrational lifetimes of the bending modes of hydrogen and deuterium defects in crystalline silicon and germanium through transient bleaching spectroscopy. They showed that the lifetimes obeyed the frequency-gap law and exhibited an exponential dependence on the decay order, validating the previously established theoretical framework. Tangentially, Kandratsenka *et al.*[14] carried out non-equilibrium molecular dynamics simulations of the VER of the two stretching and one bending modes HOD in D_2O. They found VER lifetimes of 2.7, 0.9 and 0.57 ps for the OH-stretch, OD-stretch and HOD bending respectively, where the OH-stretch has the largest frequency-gap from any accepting mode in D_2O (see FIG. 1 in their manuscript). This demonstrates that classical simulations can also reproduce the quantum mechanical principle of the frequency-gap law.

Despite the robustness of the frequency-gap law, there have been a few notable exceptions. Lüpke *et al.*[15] showed that two hydrogen defects (H_2^* and the di-vacancy defect HV · VH) within crystalline Si had VER lifetimes that differed by two orders of magnitude, despite having nearly identical frequencies. They speculated that the longer VER lifetime of the HV · VH defect arose from the larger spatial separation between the hydrogen and the surrounding silicon atoms. A few years later, West and Estreicher[16] studied the VER of a variety of hydrogen and deuterium defects (including those previously studied by Lüpke *et al.*[15]) in crystalline silicon with first principles molecular dynamics. They also found that certain defects deviated from the frequency-gap law, however, they attributed these deviations to the differences in local vibrational mode (LVM) coupling. In particular, they found the VER lifetime of the H_2^* defect was shorter than its deuterated counterpart (D_2^*). Upon closer inspection, they noted that the H_2^* defect was dissipating its vibrational energy into an LVM and a pseudo-local vibrational mode (pLVM), whereas, the D_2^* defect stretch mode was decaying into an LVM and a bulk phonon mode. They defined a pLVM as a localized mode with a frequency within the phonon continuum. Further analysis of other types of defects allowed the authors to conclude that the coupling between an LVM and

another LVM or pLVM was much stronger than the coupling between an LVM and bulk phonon modes. Additionally, Kohli *et al.*[17] studied the VER lifetime of the 1136 cm^{-1} vibration of oxygen defects in crystalline ^{28}Si and ^{30}Si. They found that the vibrational energy would decay into the symmetric-stretch of Si−O−Si, and the excess energy (the frequency difference between the donor and acceptor modes) would go into lattice modes. For cases where the excess energy was taken up by a single phonon they found that the VER lifetime would depend on the vibrational density of states (VDOS) constituted by the phonons at the frequency equal to the excess energy. In particular, the decay rate increases as the VDOS at the frequency equal to the excess energy increases. A better understanding of how LVM couplings and the VDOS can influence VER rates is necessary for a complete picture of VER theory.

In regard to CO, various pathways of vibrational energy transfer for a monolayer of ^{13}CO on an NaCl(100) surface have been investigated, with a particular focus on understanding the dynamics of vibrational energy pooling.[18–20] Vibrational energy pooling is possible because the lifetime for VER into the NaCl(100) surface is on the order of milliseconds, which is significantly larger than the time for vibrational to vibrational (V–V) energy transfer within the CO monolayer. The reason is that a large number of phonons are needed dissipate a CO stretch mode vibrational quantum, which in accordance with the energy-gap law will results in a long lifetime. Both resonant and non-resonant V–V energy transfer is relevant, i.e., the energy difference between the frequency levels of the donor and acceptor molecules being zero or non-zero, respectively. Corcelli and Tully[19] calculated the rate for resonant V–V energy transfer by assuming only a dipole–dipole coupling between parallel molecules, finding a (life-)time of 623 ps between individual resonant V–V energy transfer events. For the non-resonant V–V energy transfer from the donor molecule in a lower vibrational state pooling towards the acceptor already in a higher vibrational state, the excess energy must be taken up by a small number of phonons of the NaCl(100) surface. When only a single phonon is involved in the uptake, the corresponding lifetime varied between 1 μs and 10 ns, growing larger as the excess energy grew larger. They subsequently followed up this work with calculations of these same rates but for CO and for CO $\rightarrow$ ^{13}CO, where they found similar trends for the rates.[21]

Simulating VER in a molecular solid of a diatomic molecule (such as CO) allows us to ignore intramolecular energy redistribution, as well as constrain the number of available pathways for energy dissipation. For CO in particular, three main vibrational energy dissipation pathways are available; (i) resonant V–V energy transfer, (ii) non-resonant V–V energy transfer, and (iii) direct dissipation of vibrational energy into low-

frequency ("lattice") modes. Through isotopic substitutions we can probe the CO VER across a wide range of frequency-gap values. This allows us to scrutinize the frequency-gap law and analyze influence of the VDOS for the VER, whereby the latter aspect has never been studied in depth by dynamical simulations. Additionally, simulating the VER within amorphous and crystalline structures allows us to compare how an LVM couples to another LVM or a non-local (collective) vibrational mode. Within a crystalline CO ice the normal modes can be considered collective, consequently, isotopic substitution of the excited molecule will result in an isolated LVM. As such, VER simulations with crystalline CO allows us to study how LVM couplings affect the frequency-gap law.

We performed classical non-equilibrium molecular dynamics (NEMD) simulations of VER in solid carbon monoxide with four different isotopologues. We first show that the VER in our simulations traces the resonant (when the frequency-gap is near zero) and non-resonant V–V energy transfer pathways. Next we show how the VDOS influences the VER rate for amorphous and crystalline clusters. Finally, we discuss how the resonant V–V energy transfer is independent of isotopologue pairings, and is not restricted by the crystal structure.

6.3 Methods

All molecular dynamics simulations, data analysis and plotting was done using the Julia (version 1.9.0) programming language [22]. A variety of Julia packages were used; *Optim.jl* [23] (version 1.7.7) was used for optimizations, *LsqFit.jl* (version 0.15.0) was used for least square fittings, *FiniteDifferences.jl* (version 0.12.30) was used for calculating Jacobians, *DifferentialEquations.jl* [24] (subpackage *OrdinaryDiffEq.jl* version 6.54.0) was used for integrating the equations of motion for NEMD simulations, and *Makie.jl* [25] (subpackage *CairoMakie.jl* version 0.10.8) was used for plotting. Fast Fourier transforms (FFTs) were carried out using Julia bindings for the FFTW [26] library. Delaunay triangulations (used for calculating α-shapes) were carried out using a Julia wrapper for the Qhull [27] code.

The Jacobian used for calculating harmonic frequencies was found using a central finite difference method with 7 points (1 center point and 6 displaced points). The α parameter for the α-shape was optimized by minimizing the surface-area to volume ratio, with constraints that all points be included in the set of kept simplexes and the unique edges are a non-empty set.

We carried out molecular dynamics simulations with two different CO potentials;

a site–site interaction potential[28] and a permutation invariant polynomial neural network (PIP–NN) potential[29]. Both potentials are pair–potentials which do not include many-body effects, however, we have recently shown that for CO the many-body contributions beyond pair interactions account for less than 2% of the total interaction energy.[30] The PIP–NN potential was fit to *ab initio* data calculated with a smaller (extrapolation of double and triple zeta) basis set than what was used to fit the site–site potential (quadruple zeta), resulting in a reduction of the cohesive energy (consequently reducing the density) in the PIP–NN potential. The potential energy surface (PES) explored in the site–site potential was based on a smaller number of geometries than in the PIP–NN potential. The difference lies mainly in the smaller number of different intranuclear distances considered for the site-site potential. Recently, the reliability of the site–site potential to accurately simulate high-vibrational energy ($\nu = 40$) dynamics was brought into question.[31] Also, Chen *et al.*[29] state that their couple-cluster-based training data allows their potential to cover the lowest 33 vibrational states of the CO monomer reliably. As such, we limit the energy used for vibrational excitation in our simulations to less than 1 eV where we expect both potentials to give fully reliable results. We also note that the computational cost of the PIP–NN is more than an order of magnitude larger than the site–site potential.

Amorphous clusters were grown using an in-house "hit-and-stick" algorithm, similar to our previously used cluster growing scheme.[30] Here, we replace the optimization cycle with an NVT cycle, which employed the velocity rescaling thermostat (with a 100 fs time constant)[32]. For all NVE and NVT simulations herein the equations of motion were integrated with the velocity Verlet algorithm[33,34], using a 1 fs timestep (unless otherwise stated). We grew clusters using cycles of 5 ps for each simulation type, with the incoming molecule having 10 K translation energy directed at the center of mass of the cluster. We grew clusters of various sizes and did preliminary checks on the influence of the cluster size on the VER (see Appendix), but noted very little influence so we opted for a size of 250 molecules. Crystalline clusters were made by taking a spherical cut from the center of our previously used α–phase CO (α–CO) crystal; an 864 molecule α–CO cluster.[30] The space group and lattice parameters for our α–CO cluster are taken from literature.[35,36] The spherical cut was done with radius 13.75 Å, and isolated surface molecules were removed until the total cluster size was 250 α–CO molecules. The crystalline cluster was optimized, once with each potential, with a convergence criteria of 1×10^{-6} gradient norm. Crystalline order is unperturbed up to $\sim$ 10 Å from the center of the cluster, and no particular Miller-indices were favored for surface termination. Finally, we ran a 20 ps NVT simulation

with 10 K temperature. After preparing the clusters, we ran a 30 ps NVE simulation where a snapshot of the cluster was taken every 1.5 ps (20 total snapshots). These cluster snapshots are used to increase the variety of starting conditions to improve our statistical sampling. Isotopic substitutions for the cluster or excited molecule are done prior to the dissipation simulation.

To ensure proper statistical sampling for the energy dissipation studies, 100 trajectories have been calculated by general initial conditions in the following way: First, we randomly choose one of the 20 snapshots, then we calculate its α-shape to distinguish surface and bulk molecules. After that, we randomly select a molecule within the desired region, if applicable, we swap the mass of the selected molecule or of the cluster and then run a 10 ps NVE simulation to equilibrate the system. The selected molecule is subsequently excited to a specific vibrational energy by increasing the momenta of its atoms along the eigenvector of the mass weighted Hessian (calculated as an isolated molecule). A 1.5 or 2 ns (depending on the potential used) NVE simulation is carried out to monitor the VER of the excited molecule.

We study the VER of four different isotopologues, $^{12}C^{16}O$ (referred to simply as CO), $^{13}C^{16}O$, $^{12}C^{18}O$, $^{13}C^{18}O$, within clusters composed exclusively of one of these isotopologues. We adopt the following naming convention Excited–phaseCluster; where Excited is the isotope of the excited molecule, phase is the structural phase of the cluster (am = amorphous; cry = crystalline), and Cluster is the isotope of the cluster molecules. For example, CO–amCO denotes an excited $^{12}C^{16}O$ molecule within an amorphous $^{12}C^{16}O$ cluster.

We calculate the radial distribution of clusters by taking the distances between the center-of-mass of CO molecules. Similarly, we use the angle between CO molecular axes for calculating the angular distribution of clusters. We evaluate the degree of delocalization of each CO-stretch mode through the inverse participation ratio (IPR)

$$\rho_i = \frac{(\vec{u}_i \cdot \vec{u}_i)^2}{(\sum_j^N \vec{u}_j \cdot \vec{u}_j)^2} \quad . \tag{6.1}$$

Here $N = 250$ is the number of molecules in each cluster. The ($6N$ =) 1500-dimensional displacement vector $\vec{u}$ associated with the CO-stretch mode of each molecule is obtained from the harmonic frequency calculations. $\vec{u}_j$ denotes the six components describing the displacements of molecule j for this particular normal mode. For each CO stretch mode, we calculate the number of participating molecules for this mode by counting all ρ_i values larger than $\frac{1}{250^2}$. Here, $\rho_i = \frac{1}{250^2}$ corresponds to all molecules participating equally, ie., perfect delocalization of this mode, whereas for $\rho_i = 1$ the

mode is fully localized on a single CO molecule. The number of participating molecules is calculated for all CO stretch normal modes across all snapshots, resulting in $250 \cdot 20 = 5000$ values for each configuration (potential and cluster type).

Following a similar methodology as previously used[37], we calculate the vibrational coupling parameter between pairs of CO molecules. The vibrational coupling parameter (β)[38] is given by

$$\beta = \frac{\partial}{\partial r_\nu} \ln(V + 2\epsilon) \quad , \tag{6.2}$$

where V is the intermolecular interaction potential, ϵ is the well depth (preventing the argument of the logarithm to become negative), and $\frac{\partial}{\partial r_\nu}$ is the partial derivative with respect to the vibrational mode. Here we use the dimer well depth calculated using the PIP–NN potential ($\epsilon = 130$ cm^{-1}). In order to sample a distribution of coupling parameters relevant to our VER simulations we sample pairs of CO molecules within the bulk of a cluster at 200 different timesteps of an NVE simulation. Pairs of CO molecules were selected by taking molecules with centers of mass less than 4 Å apart.

The vibrational density of states (VDOS) of clusters was obtained by making use of the velocity autocorrelation function (VACF). For each snapshot (20 per cluster type) we ran a 75 ps NVE with 1 fs timestep, from this trajectory we calculated the VACF across 15 ps windows ($5 * 20 = 100$ total VDOS). We normalized the VACF, then applied a von Hann window[39], 8 factor zero-padding, and mirroring. An FFT was then carried out to produce a VDOS, and finally all 100 VDOS were averaged to a single VDOS.

We investigate energy interconversion by taking the average vibrational, translational and rotational energy per non-excited molecule, then further averaged across the 100 trajectories. The vibrational energy is calculated by taking both the intramolecular potential energy and the kinetic energy component of vibrational motion, whereas rotational and translation energies do not include their potential energy counterparts.

6.4 Structural and Vibrational Properties

Table 6.1 compiles the vibrational frequencies of all isotopologues as isolated molecules in the gas phase, using both interaction potentials under the harmonic approximation. While the absolute frequencies differ from experimental ones, the calculated frequency-gap $\Delta\nu$ relative to CO is at most 3 cm^{-1} off from the corresponding experimental frequency gap values. In the context of the VER simulations carried out in our work, the frequency-gap holds significantly more importance than the absolute frequencies. As

Table 6.1: Gas-phase vibrational frequencies (cm^{-1}) of the four isotopologues used in this study and their shifts $\Delta\nu$ (cm^{-1}) with respect to CO. For both potentials the frequencies are calculated from isolated molecules *in vacuo*, and using the harmonic approximation. The experimental values are gas-phase measurements.

Isotopologue	Site–Site		PIP–NN		Experiment [40]	
	ν	$\Delta\nu$	ν	$\Delta\nu$	ν	$\Delta\nu$
CO	2196	0	2169	0	2139	0
^{13}CO	2148	48	2121	48	2092	47
C^{18}O	2143	53	2116	53	2088	51
^{13}C^{18}O	2094	102	2067	102	2040	99

such, the worse agreement between absolute theoretical and experimental frequencies is not expected to be a significant source of error in the VER simulations.

In the top two panels of Figure 6.1 the radial (left) and angular (right) distributions of the amorphous and crystalline clusters are shown based on the site–site potential. All features are qualitatively identical also for the PIP–NN potential (see Appendix). As expected, the radial distribution for the crystalline clusters shows increased short-range ordering (see also Karssemeijer *et al.* [41]), whereas the long-range component is in better agreement with the amorphous distribution due to less well-ordered surfaces dominating the former at long distances. The sharpest contrast between the two structures is seen in the angular distributions, where the crystalline distribution shows two distinct peaks centered at 11 and 109 degrees. Distributions of the number of participating molecules per vibrational mode for crystalline and amorphous clusters is shown in the bottom panel of Figure 6.1. The crystalline distribution is trimodal with one peak being more non-local than the amorphous distribution, although it still contains a strongly localized peak because of the lack of periodic boundary conditions.

Figure 6.2 shows the low frequency vibrational density of states (VDOS) for a crystalline and amorphous CO cluster with both the site–site and PIP–NN potentials. The low frequency component of the VDOS is not significantly affected by the cluster isotopologue, as such, we only show the VDOS of CO clusters. It is worth discussing the differences in the low frequency modes predicted by each potential, however, an in-depth discussion and highly accurate phonon band are beyond the scope of this paper. Both potentials yield broad Lorentzian bands centered around 35 cm^{-1} for amorphous clusters, with the PIP–NN potential having a slightly longer tail. These are in good agreement with experiments that observe a broad Lorentzian band centered at 50 cm^{-1}.[42] For the crystalline clusters the two vibrational spectra are more different, however, they both still exhibit two distinct peaks at roughly 45 cm^{-1} and 80 cm^{-1}.

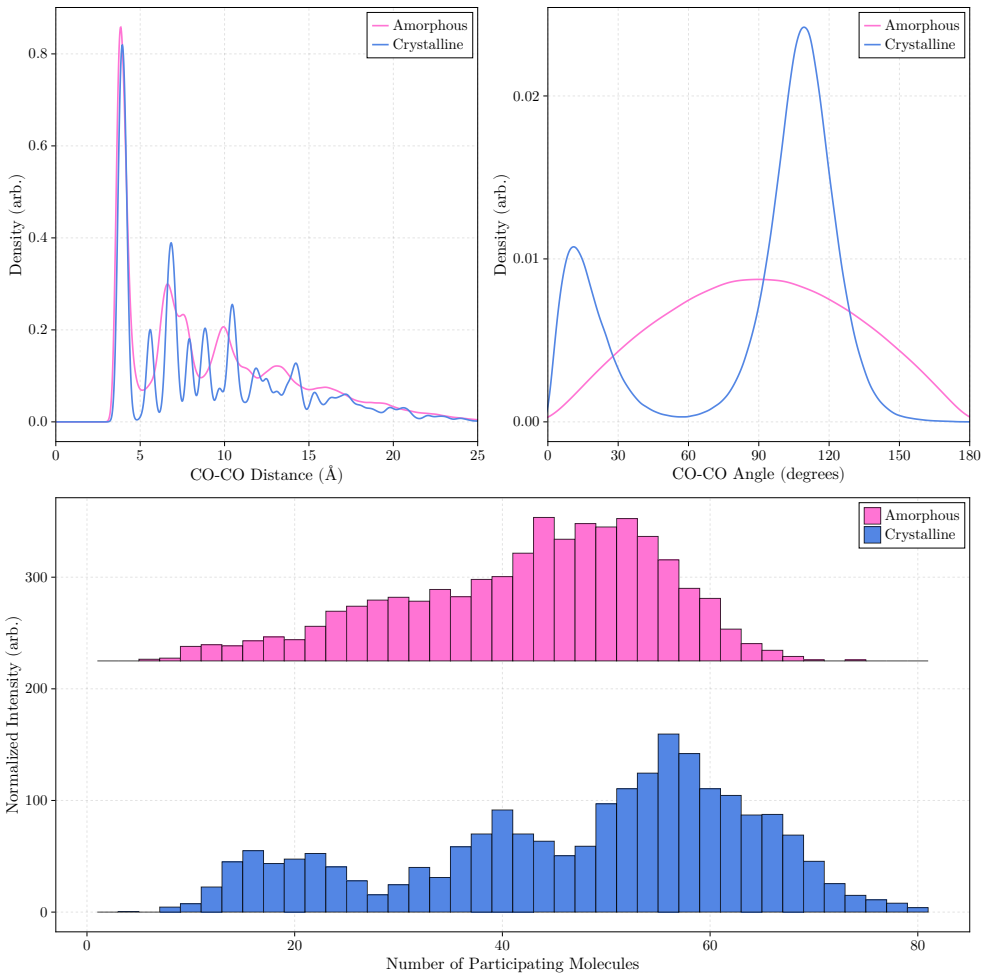

Figure 6.1: Comparison of geometric and vibrational properties from 10 K clusters made using the site–site potential. Top Left: radial distribution of CO molecules in amorphous (pink) and crystalline (blue) clusters. Top Right: angular distribution between CO molecules in amorphous (pink) and crystalline (blue) clusters. Bottom: number of participating molecules for the CO stretch vibrations in amorphous (pink) and crystalline (blue) clusters. The amorphous distribution is offset by 225 for visual clarity.

In close agreement with THz measurements of α-CO, which show one peak centered at 50 cm^{-1} and another at 80 cm^{-1}.[43]

A distinct difference in the two potentials is the sharp peak towards 0 cm^{-1} for the crystalline cluster using the PIP–NN potential. Peaks at 0 frequency are usually caused by so-called "bias" in the "signal" that undergoes the Fourier transform step in the

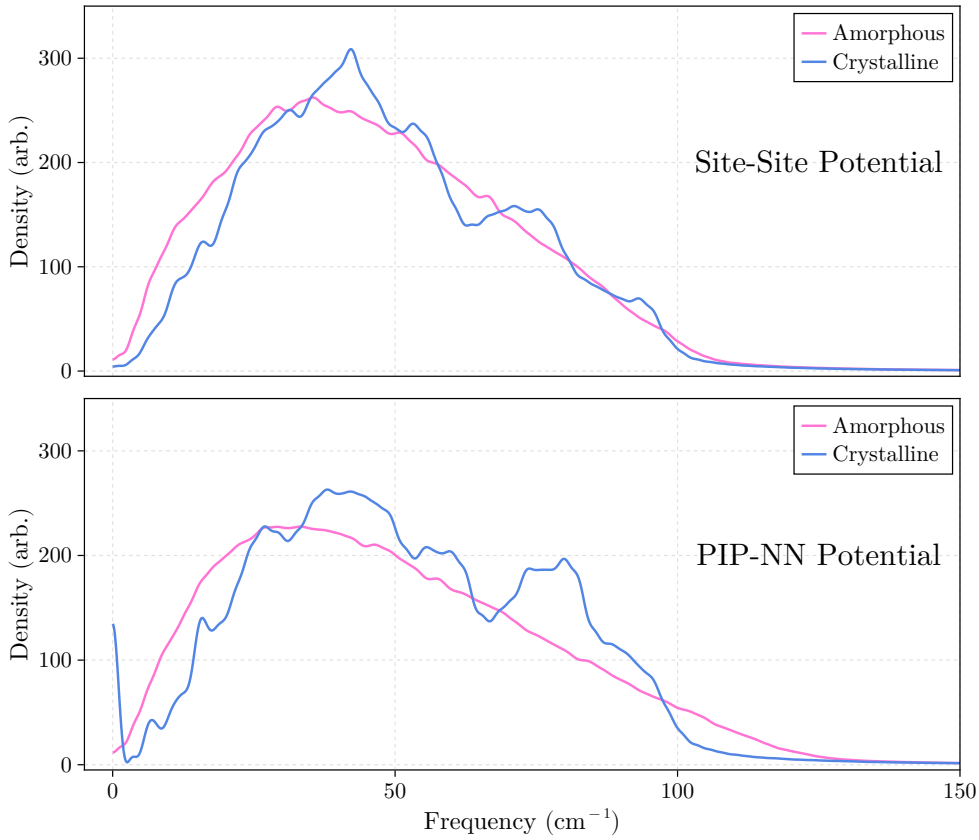

Figure 6.2: Low-frequency part of the vibrational density of states (VDOS) of amorphous (pink) and crystalline (blue) CO clusters with (top) the site–site potential and (bottom) the PIP–NN potential.

VACF calculation. In all spectra shown here this has been dealt with by subtracting the mean from the signal, however, for some of the crystalline clusters with the PIP–NN potential a bias remained. A source of bias that is not fully removed by the aforementioned procedure is cluster restructuring towards a different local minimum. Where the conversion of potential energy into kinetic energy can result in a bias in the VACF signal not equal to the signal mean. Peaks caused by bias in the signal typically have the largest density, since the observed peak is not the largest it means only a few trajectories used to calculate the VDOS present restructuring. Since our results are taken from the ensemble average of 100 trajectories, any influence of restructuring on the VER will be negligible in the ensemble average. As such, we do not suspect it to

have caused any differences in the results of the PIP–NN potential as compared with the site–site potential.

The structural and vibrational properties shown in Figures 6.1 and 6.2 display the key differences between the two clusters types, and any differences in the VER between amorphous and crystalline clusters must be explained by one of these differences.

6.5 Analyzing Vibrational Energy Relaxation with Classical Dynamics

6.5.1 Trajectory Ensembles

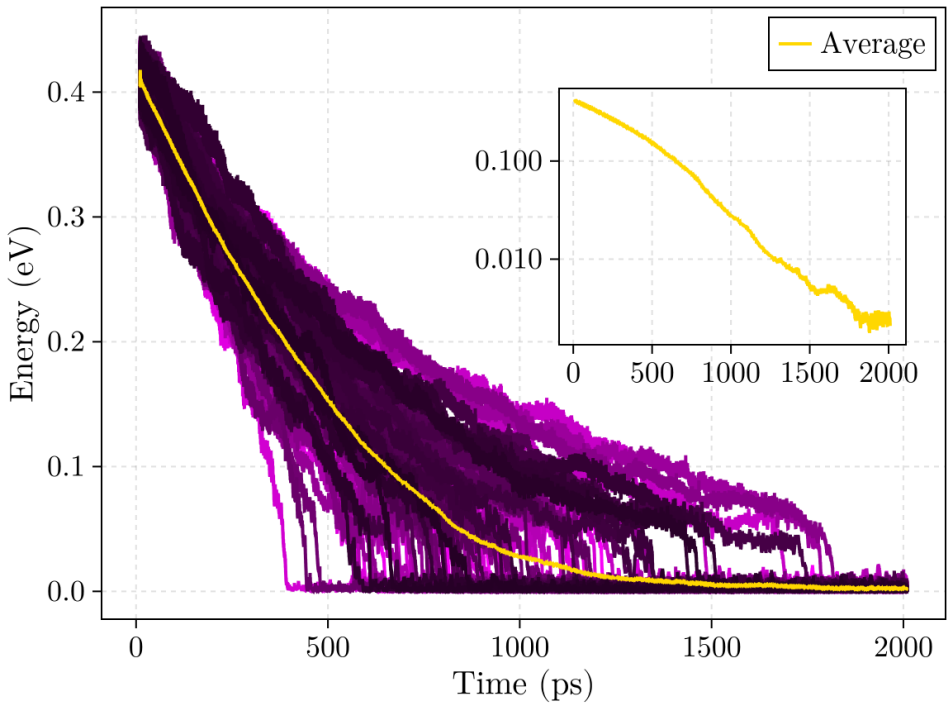

Figure 6.3: Vibrational energy dissipation for CO–amCO simulations with the site–site potential. All 100 trajectories are shown in purple, and the average of them is shown in gold. Inset plot shows only the average energy decay with the a logarithmic y-axis.

All results discussed herein are ensemble averages of 100 trajectories, as shown by Figure 6.3. Individual trajectories (purple lines) generally show very similar shapes,

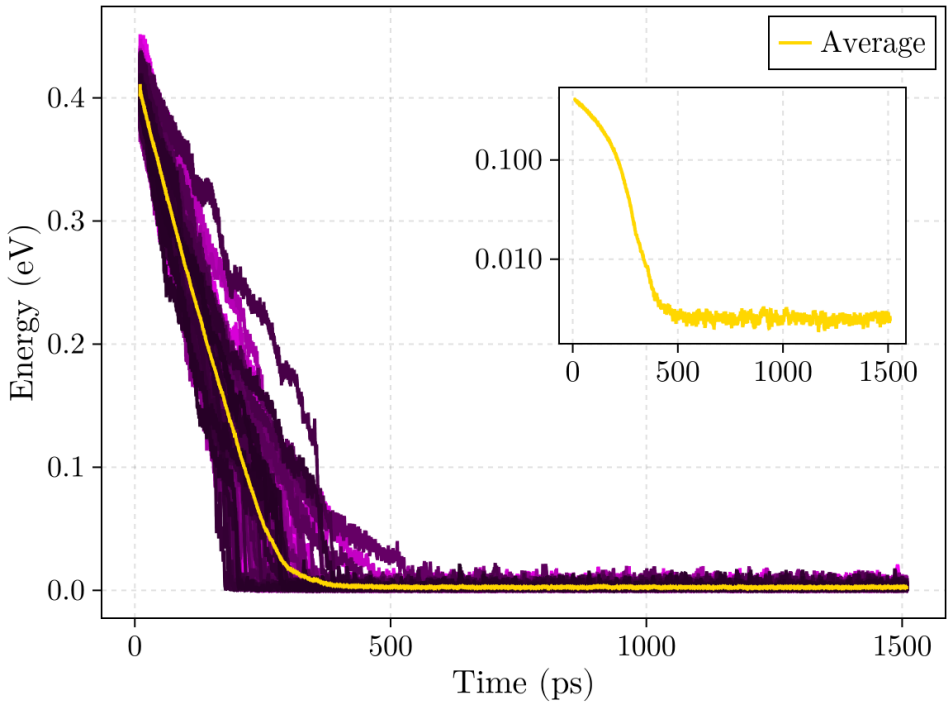

Figure 6.4: Same as Figure 6.3 but using the PIP–NN potential.

however, there is a broad range of lifetimes (spanning roughly 500 to 1500 ps). Their average (gold line) is used to determine the time dependent vibrational decay rates. Figure 6.3 shows the results of simulations for CO–amCO using the site–site potential, Figure 6.4 is the equivalent plot for the corresponding configuration obtained with the PIP–NN potential. In both cases, these trajectories are for "self-dissipation", i.e., an isotope within a cluster of the same isotope, which results in a resonant energy transfer event at low energies (*vide infra*). In the Appendix another representative example is provided for CO–cryCO (using the site–site potential).

Across all simulations, the PIP–NN potential produces faster relaxation rates than the site–site potential. To better understand how the vibrational coupling differs in each potential, we calculated the vibrational coupling parameter between neighboring CO molecules. Figure 6.5 shows the kernel density estimation of the distribution of vibrational coupling parameters found for each potential. The average vibrational couplings are -0.0156 a_0^{-1} for the site–site potential, and -0.0218 a_0^{-1} for the PIP–NN, which is in agreement with the shorter relaxation lifetimes observed with the PIP–NN

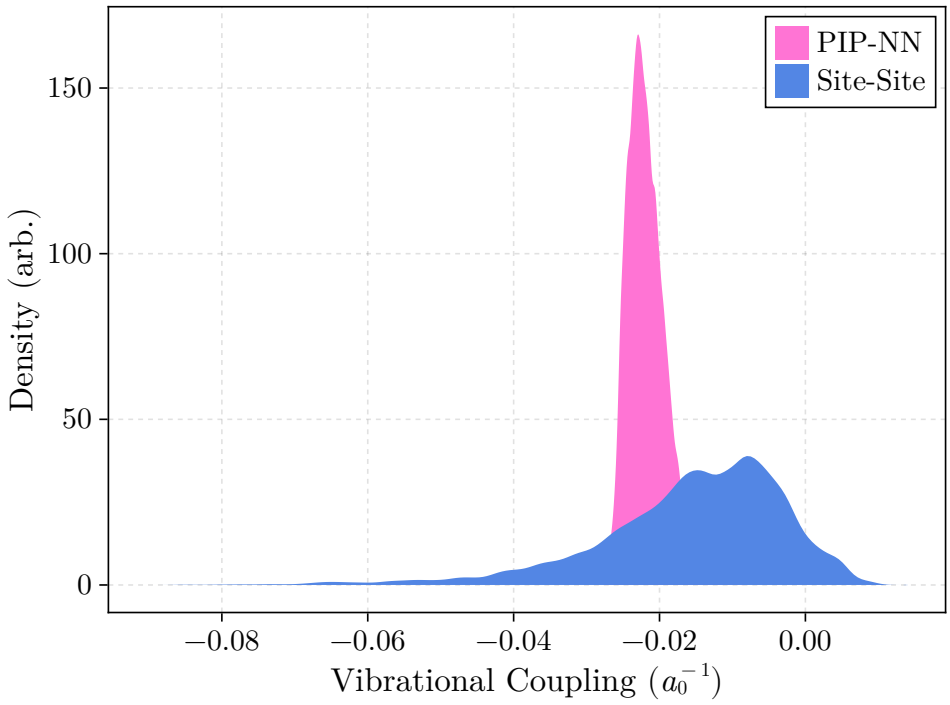

Figure 6.5: Vibrational coupling parameter for pairs extracted from amorphous clusters.

potential. Furthermore, the site–site potential produces a much broader distribution of couplings than the PIP–NN potential. This is reflected in the broad range of VER lifetimes seen across the 100 trajectories using the site–site potential (see Figure 6.3) compared to the trajectories using the PIP–NN (see Figure 6.4).

6.5.2 Frequency Shift

For diatomic molecules described by intramolecular Morse potentials, the excited frequency for a given excitation energy is given by[44]

$$\nu^\star = \nu_\circ \sqrt{\frac{D-E}{D}} \quad , \tag{6.3}$$

where $\nu^\star$ is the excited frequency, $\nu_\circ$ is the frequency of classical small vibrations, D is the dissociation energy and E is the vibrational energy. Since this equation was derived for a single Morse potential, it does not include many-body effects resulting

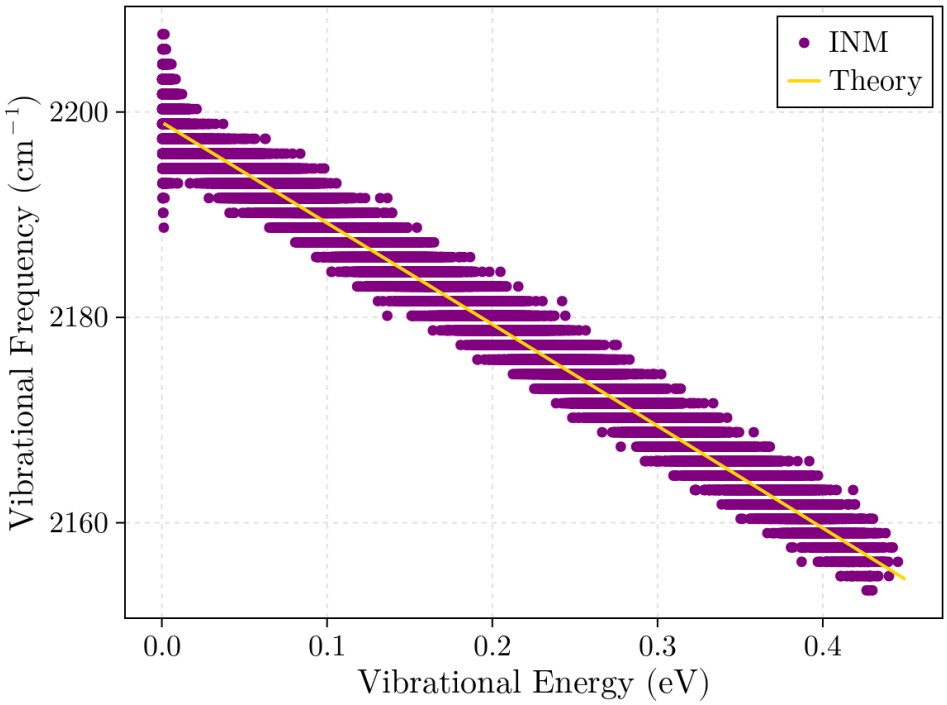

Figure 6.6: INMs (purple dots) of an excited CO molecule within an amorphous $(CO)_{250}$ cluster versus the vibrational energy of the excited molecule. The predicted excited frequency for given a vibrational energy is shown in gold (see Equation (6.3)). All data from 100 trajectories using the site–site potential are shown.

from intermolecular interactions. To confirm this holds for a molecule within a cluster, we calculate the instantaneous normal mode (INM) of the excited molecule including the interactions with all other molecules at every picosecond of the simulation. The INMs were calculated by running a short NVE simulation (50 fs with 0.01 fs time step) at each picosecond, then taking the bond length of the excited molecule during this NVE. This bond length array was then sliced between the first three turning points (one full wave), then repeated 1000 times and run through an FFT algorithm to get the INM of the excited molecule. Figure 6.6 shows the INMs (purple dots) of the excited molecule (across all 100 trajectories of the CO–amCO simulations) across the full simulation, as well as the predicted frequency shift based on Equation (6.3) (gold line). For the predicted frequency shift $\nu_\circ$ was set as the mean INM (roughly 2199 cm^{-1} for Figure 6.6) after the vibrational energy had equilibrated with the cluster. A

range of frequencies per vibrational energy is observed in the INMs due to the large configurational space sampled.

Excellent agreement between the predicted frequency and the calculated INMs reveals that intermolecular contributions are negligible in the frequency shift of excited CO. The PIP–NN potential also yields a perfect agreement between predicted frequency and calculated INM. As such, we can calculate the INM of our ensemble average (*vide infra*) by using Equation (6.3) with $\nu_\circ$ set to the mean INM of the excited molecule prior to excitation. We can then calculate the instantaneous frequency-gap

$$\Delta\nu = \nu^\star - \nu_{\text{clu}} \quad , \tag{6.4}$$

where ν_{clu} is the mean frequency of the cluster. In this formalism a negative frequency-gap implies an excited molecule frequency lower than that of the cluster frequency.

6.5.3 Frequency-Gap Dependent Decay Rate

A consequence of the frequency-gap law is a non-exponential decay in the slow regime, where the VER is slow enough to allow the decay rate to change as the frequency changes. Goldstein and Bialek[45] derived an expression for radiationless transitions in the slow regime, and found that the decay rate may increase or decrease over the course of the transition. This is particularly important for classical simulations where the frequency of the excited molecule shifts (shifting the frequency-gap) during the dissipation process, resulting in a non-constant decay rate. Zhang *et al.*[46] speculated that this phenomenon was occurring in the VER of DF in CD_2Cl_2, more specifically, as the DF dissipated its energy the vibrational frequency red-shifted resulting in less spectral overlap with the solvent. When they fit an exponential to the first 5 ps of the time evolution of the vibrational energy they found a time constant of 7.6 ps, whereas, fitting the full time evolution gave a time constant of 8.8 ps. For systems with strongly coupled excited and accepting modes the variation in the decay rate is negligible and a typical exponential decay is still produced. This is not the case for the CO clusters studied here, where the coupling is weak and the variation in the decay rate is quite large. Consequently, fitting an exponential decay to the time evolution of the original excitation extracted from our NEMD simulations is insufficient, and we have developed a new procedure instead. Below we describe our procedure for calculating pseudo-instantaneous decay rates.

For short timescales the frequency-gap shift is negligible, which in turn results in a nearly constant decay rate. As such, within short timescales the vibrational energy

decay can be fit with the typical exponential decay function

$$E(t) = E_{\circ} e^{-\frac{t}{\tau}} \quad , \tag{6.5}$$

where $E_{\circ}$ is the initial excitation energy, τ is the decay time constant and t is the simulation time. Note, the decay time constant is a pseudo-instantaneous value related to the time dependent vibrational decay rate. As such, it should not be confused with typical exponential lifetimes found by fitting across the full simulation time. To get the decay time constant as a function of simulation time we employed a fitting procedure analogous to the Savitzky-Golay filter[47] algorithm. We fit a standard exponential (Equation (6.5)) to successive adjacent subsets (of length N) of the energy decay, where each new subset differs by only 1 data point (corresponding to 1 fs in the simulation time). The fitted decay time constant is then attributed to the time corresponding to the first data point in the subset. When the standard error in the decay time constant became larger than 5% of the fitted decay time constant the algorithm was terminated and no new subsets were included in the fitting procedure. The only variable parameter in this method is the subset length (N), which if set too large (or too small) would result in large oscillations of the decay time constant. We carefully selected the length to reduce the oscillations, and in general found values between 400 and 850 to be ideal.

6.6 Results and Discussion

6.6.1 Amorphous Cluster

Figure 6.7 shows the decay time constant as a function of the frequency-gap between the excited molecule and the amorphous cluster for both potentials. Both potentials produce similar frequency-gap dependencies, where τ increases as the frequency-gap increases. Across the entire frequency-gap range we studied, the site–site potential produces larger τ values compared to those produced by the PIP–NN potential. Inline with our findings that the PIP–NN potential has a stronger average coupling strength (see Figure 6.5) for vibrational modes. Unlike the site-site potential the PIP–NN potential does not allow to decompose these couplings into contributions from different interactions. In fact, the total energies from the quantum chemical calculations, which it has been fitted against, do not feature such a decomposition. Electrostatic interactions typically represent the strongest portion of vibrational coupling, however, in the case of CO its the weakest contribution to the intermolecular interaction in the

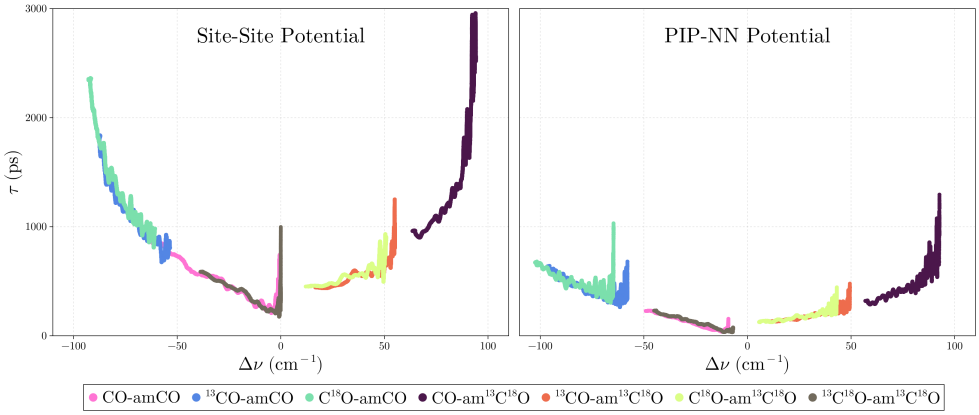

Figure 6.7: Vibrational energy decay time constant as a function of frequency-gap for amorphous clusters using the site–site potential (left) and the PIP–NN potential (right). Various isotopologue configurations are included in the figure, where the isotopologue-induced frequency shifts help cover a larger frequency-gap range. A larger excitation energy (0.6 eV) was used for the CO-amCO case (pink) in the site–site potential, which results in a larger frequency gap range than other curves. The frequency-gap was calculated through the excited molecules vibrational energy, as explained in Section 6.5.2. The $^{13}C^{18}O$-amCO case was excluded from the plot due to the decay time constant produced by both potentials being extremely large.

site–site potential.[30] This should be consistent within the PIP–NN training set data, nevertheless, the PIP–NN potential clearly exhibits an enhanced vibrational coupling when compared with the site–site potential.

Despite the faster VER with the PIP–NN potential, both potentials provide qualitatively similar results. An offset between the curves for negative and positive frequency gaps is seen in Figure 6.7 for both potentials, indicative of an enhancement of the VER rate when the excited frequency is lower than the accepting mode frequency. The magnitude of the offset diminishes as the frequency-gap increases, with decay time constants at gaps above 50 cm^{-1} being essentially equal to their negative counterparts. Incidentally, this is also where the excited molecule is a different isotopologue compared to the cluster; making it possible that this enhancement is not inherent to the sign of the frequency gap, but rather due to the isotopic combinations. Following this logic, it would appear that the offset is a result of a different anharmonic coupling, possibly produced by the differing degrees of LVM character, between isotopologues.

With both potentials the decay time constant for $^{13}C^{18}O$-amCO was so large that the total energy dissipated was negligible across the total simulation time of 1.5 or 2 ns. This is in line with recent experimental findings that showed how vibrational energy

could be transported in the CO → $^{13}C^{18}O$ direction but the reverse was not possible.[48] However, the exact mechanism constraining the allowable direction of energy transfer in experiments is different compared to our simulations. In the experiments the lack of thermal energy sufficient enough to compensate the higher energy vibration of CO over $^{13}C^{18}O$ produces the constraint. In contrast, for our simulations this arises from the large frequency-gap producing an extremely weak vibrational coupling, resulting in a negligible energy transfer rate.

6.6.2 Crystalline Cluster

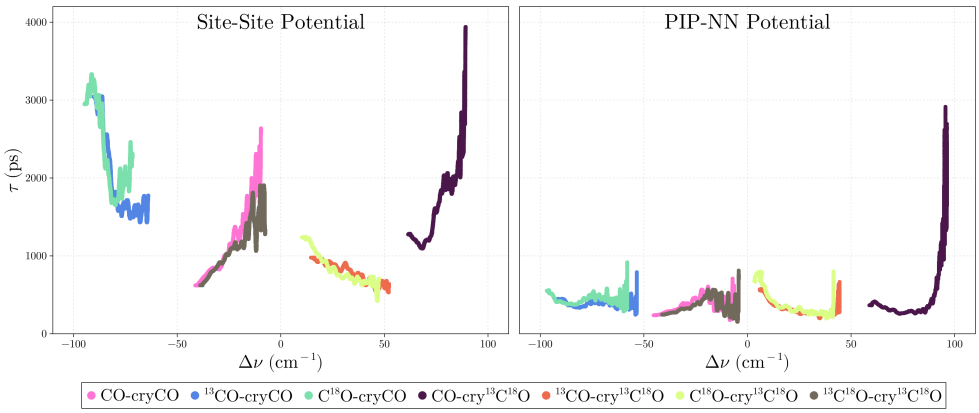

Figure 6.8: Same as Figure 6.7 but for crystalline clusters.

Figure 6.8 shows the decay time constant as a function of the frequency-gap between the excited molecule and the crystalline cluster using the site–site (left) and PIP–NN (right) potentials. As was the case for the amorphous clusters (see Figure 6.7), both potentials again produce similar trends with the PIP–NN having smaller τ values. Furthermore, both potentials produce very similar structures and distributions of participating molecules for both amorphous and crystalline clusters (see Figure 6.1 and Figure S3 in the Appendix). One peculiarity in the crystalline case is the asymmetry in the PIP–NN potential, where the CO–cry$^{13}C^{18}O$ simulation has a much stronger frequency-gap dependence.

Within the -50 to 50 cm^{-1} frequency-gap range the crystalline clusters exhibit a different frequency-gap dependence than the amorphous clusters. This is observed in both potentials, however, it is less drastic in the PIP–NN potential. Across the entire frequency-gap curve for each cluster configuration the degree of LVM–LVM

coupling is reduced, as such, changes localized to certain frequency-gap ranges are not directly resulting from the diminished LVM–LVM coupling. At small frequency-gaps the excited molecule couples strongly to a nearby molecule, and can even resonantly transfer vibrational energy. This resonance is not captured by the τ values in Figure 6.8 due to the resonant energy transfer (discussed in more detail in Section 6.6.5) not producing an exponential energy decay curve. As such, our methodology for producing frequency-gap dependent decay rates does not produce τ values at these frequency-gaps.

6.6.3 Analysis of Energy Redistribution

Although clearly not the goal of this study, it is instructive to do an order-of-magnitude comparison with what has been found for CO adsorbed on NaCl(100) before going into a more detailed analysis: In all configurations involving different CO isotopologues we studied, the VER lifetime is near the nanosecond regime. This is several orders of magnitude different from direct VER of a CO vibrational quantum into lattice modes – and thus indicative of V–V energy transfer rather than direct dissipation. On the other hand, the VER lifetime for converting one CO vibrational quantum into lattice modes of NaCl(100) and solid CO could be very different. For the resonant V–V energy transfer Corcelli and Tully [19] found a lifetime of 623 ps, which is fairly similar to the lifetime observed in our simulations. However, most of our simulations are with mixed isotopologues and thus do not meet the conditions required for resonant V–V energy transfer. For single-phonon non-resonant V–V energy transfer, Corcelli and Tully [19] obtained lifetime between 10 ns and 1 μs. Their quantum mechanical model assumes parallel CO molecules described as interacting dipoles. In contrast, our simulations are classical for non-parallel-oriented assemblies of CO molecules, and both interaction potentials go clearly beyond dipole-dipole interactions. The ensuing detailed analysis of the energy redistribution allows to better understand which energy transfer processes are (predominantly) described by our simulations.

Figure 6.9 shows the average energy gained per non-excited molecule during CO–amCO and CO-cryCO VER simulations with each potential, decomposed into kinetic and potential energy contributions of intramolecular vibrations (V) together with kinetic energy contributions of translations (T) and rotations (R). We only include simulations of CO VER within CO clusters since all other simulations for different isotopologue combinations (with both potentials) revealed similar trends.

Although not directly visible in Figure 6.9, we note in passing that the average total

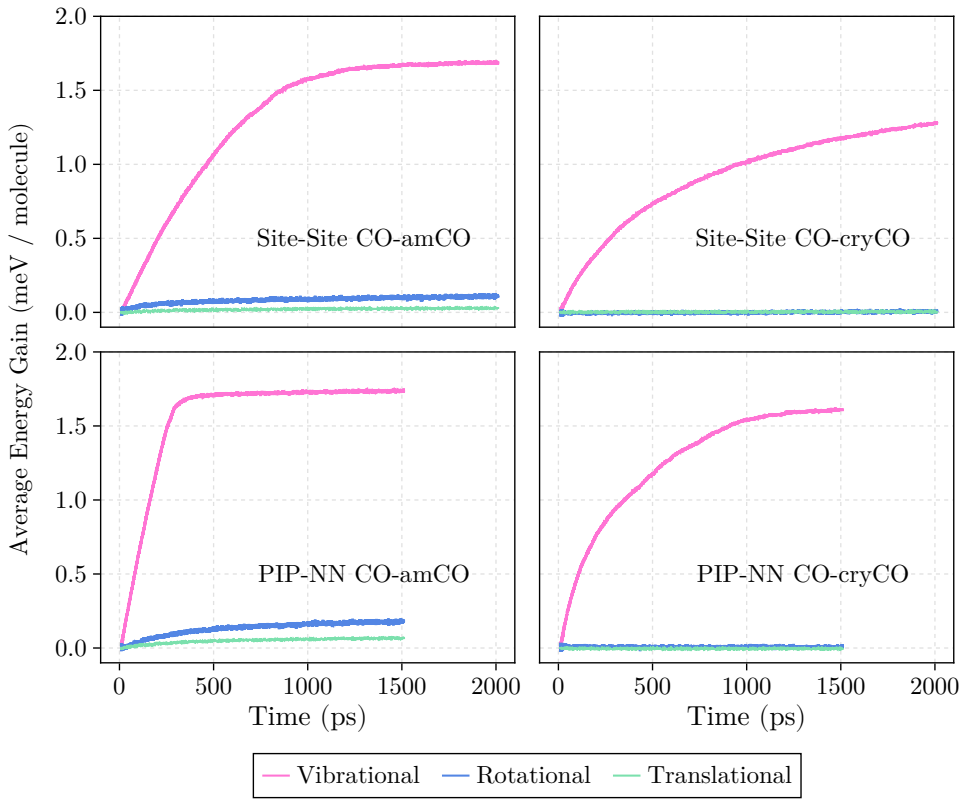

Figure 6.9: Average energy gained per molecule during a site–site CO–amCO (top-left), site–site CO–cryCO (top-right), PIP–NN CO–amCO (bottom-left), and PIP–NN CO–cryCO (bottom-right) simulation.

energy gained ($V + T + R$) is larger than the 0.4 eV excitation energy by 60 meV for the CO–amCO and 5 meV for the CO-cryCO clusters. We confirmed that the total energy is constant during each trajectory, hence, this is not a result of issues with the time integration algorithm of our NEMD simulations. Further analysis reveals that during the simulation potential energy is converted to translational or rotational kinetic energy due to structural reorganization, i.e. transition towards a different local minimum in the weakly bound clusters. The smaller average total energy gain for the crystalline clusters can be rationalized by the fact that they are intrinsically more stable: While molecules in the bulk of the amorphous clusters can contribute to the "minima hopping" by reorienting, only molecules at the edges of the crystalline clusters (can) do the same.

Most importantly, Figure 6.9 reveals that only a very small amount of the vibrational excitation is transformed into rotational and translational energy of the surrounding CO molecules. Since the latter constitutes the low-energy "lattice" modes of all clusters, our simulations are clearly not dominated by direct VER via multiphonon processes. In other words, the difficulty in converting high frequency vibrational energy into translational or rotational energy is consistent with the frequency-gap law. Instead, fractions of vibrational quanta are predominantly transferred to the vibrational stretch modes of the surrounding CO molecules, which can be seen as a realization of V–V energy transfer pathways within our classical simulations. In what follows we further analyze the non-resonant and resonant energy transfer pathways in our trajectory ensembles, whereby the former should also involve energy uptake by low-energy "lattice" modes.

6.6.4 Non-Resonant Energy Transfer

Originally motivated by the frequency-gap law, we have taken a bird's eye view at the data for the lifetimes τ presented in Figure 6.7 and attempted to fit exponential functions. Not (further) distinguishing between the different isotopologue combinations, the result for amorphous clusters (i.e., all the data included in Figure 6.7) is shown in Figure 6.10. Both a single exponential (pink) and a linear combination of two exponentials (blue) has been used, including a y-intercept constant since the τ data appears to have a non-zero asymptote. For positive frequency shifts ($\Delta\nu > 0$), it is clear that the bi-exponential fit is better than the one based on a single exponential for both interaction potentials over the entire range. For the negative frequency shifts ($\Delta\nu < 0$), the bi-exponential is favorable at least for the Site–Site Potentials at large $|\Delta\nu| > 80$ cm^{-1}. The best two exponential fit for the negative shifts using the PIP–NN potential is two half amplitude exponentials equal to the single exponential fit. As such, the two exponential fit is plotted over the single exponential (hence the lack of a pink line) fit for the bottom right panel of Figure 6.10.

If the frequency-gap law would provide a good description, only a single exponential should have been required for the fit, with the decay constant of this exponential reflecting the multi-phonon order of the direct dissipation process to low-frequency modes. Furthermore, we have also looked at the intersection points of the bi-exponentials (see Appendix): Focussing on $\Delta\nu > 0$, it is interesting to note that the intersection occurs at $\Delta\nu \approx 100$ cm^{-1} for both interaction potentials. It coincides with the tail of the VDOS for the low-frequency modes (see Figure 6.2 and decomposition

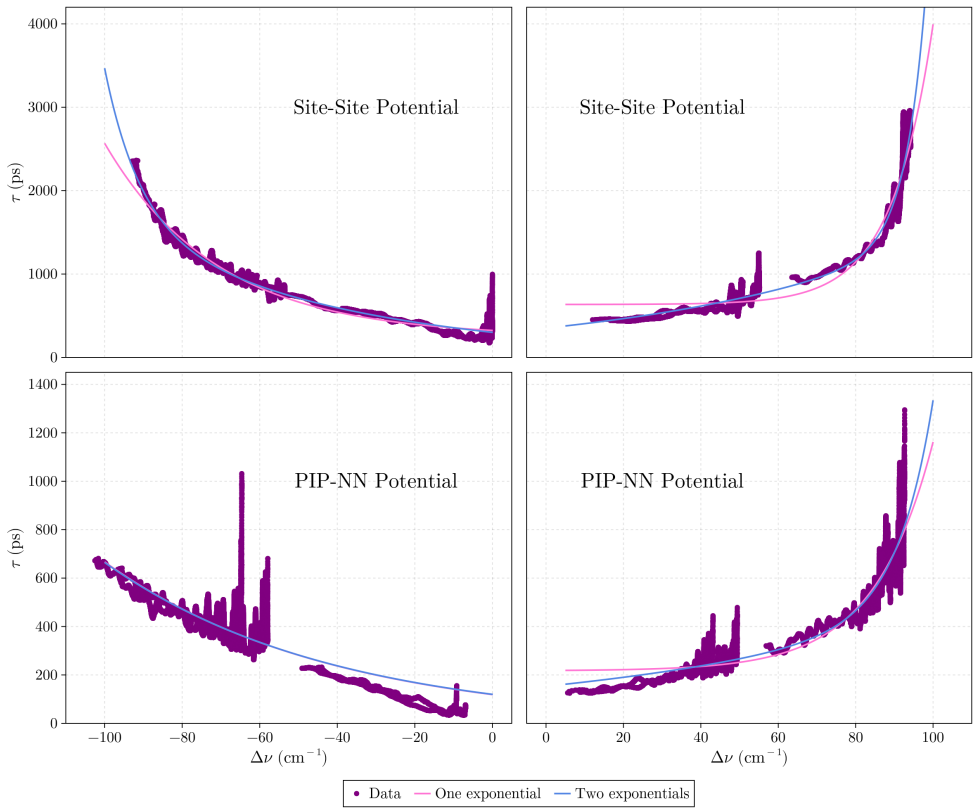

Figure 6.10: Least square fitting of the vibrational energy decay time constant as a function of frequency-gap for amorphous clusters using the site–site potential (top two panels) and the PIP–NN potential (bottom two panels). The data (purple) was fit with both a single exponential (pink) and a linear combination of two exponentials (blue).

into bulk and surface modes in the Appendix). In other words, as soon as the excess energy connected with $\Delta\nu > 0$ (see Equation (6.4)) does no longer "fit" to the energy equivalent of the maximum low-frequency mode, the $\tau(\Delta\nu)$ dependence changes. This is consistent with the non-resonant V–V energy transfer pathway suggested by energy redistribution analysis presented in the previous section: The quantum-mechanical expressions derived by Corcelli and Tully [19] for CO adsorbed on NaCl(100) result in a change of the $\tau(\Delta\nu)$ dependence when switching from one to two (or more) low-frequency mode (phonon) quanta during the non-resonant V–V energy transfer.

A similar bird's eye view on the data for the crystalline clusters shown in Figure 6.8 is complicated by the fact that τ decreases as the frequency-gap approaches

$|\Delta\nu| = 50$ cm^{-1}. It is interesting to note that this is roughly where both potentials produce a peak in the VDOS. In other words, the highest VER rate coincides with the highest density of phonon states, which is in line with the observations of Kohli *et al.*[17] for the VER of oxygen defects in crystalline silicon. Contrary to the crystalline clusters, both potentials produce the smallest τ values near zero frequency-gap despite the VDOS of the amorphous clusters peaking near 35 cm^{-1}. Decomposing the VDOS into contributions from only surface or bulk atoms, it turns out that the frequency range between 10 and 30 cm^{-1} is dominated by the surface for the crystalline clusters , whereas for the amorphous clusters the contribution from the bulk is much more pronounced in the same frequency range (see Appendix). Given that the excited molecule is within the bulk of the cluster, this disparity in bulk states could be responsible for the different behavior of the VER rate in the interval $|\Delta\nu|$ between ± 50 cm^{-1}.

6.6.5 Resonant Energy Transfer

As detailed in Section 4, none of the VER simulations underlying Figures 6.7 and 6.8 start with a zero frequency gap due to the anharmonic shift of the excited CO molecule. To deliberately make $\Delta\nu$ vanish at the beginning of the trajectories, we have run additional VER simulations for CO-am^{13}CO, Exciting the CO molecule by 0.6 eV of vibrational energy yields essentially the same vibrational stretch frequency as the average of ^{13}CO host cluster. Figure 6.11 shows all the trajectories (purple) and the average (gold), where its possible to see that for all trajectories the excited molecule loses roughly 0.2 eV in vibrational energy in the first 200 ps. Once the frequency mismatch becomes large again, i.e., the initial resonance condition is lost, the VER slows down significantly (see Figure 6.11).

We have observed the same resonant energy transfer phenomenon also in crystalline clusters (not shown). In both amorphous and crystalline it occurs in all 100 trajectories. This implies that it is independent of the cluster structure and thus the relative orientation of the CO molecules. Instead, it really only depends on the frequency mismatch. Furthermore, the average energy redistribution for the entire trajectory reveals that energy is dominantly transferred into the stretch vibrations of the neighboring molecules, in the same way as it is shown in Figure 6.9 - albeit much faster initially. Consequently, we interpret the initial parts of these simulations as classical manifestations of resonant V–V energy transfer, switching over to non-resonant V–V energy transfer during the remainder of the trajectories. The decay time constants on the order of ≈ 100 ps that we observe for the former is again consistent with the quantum

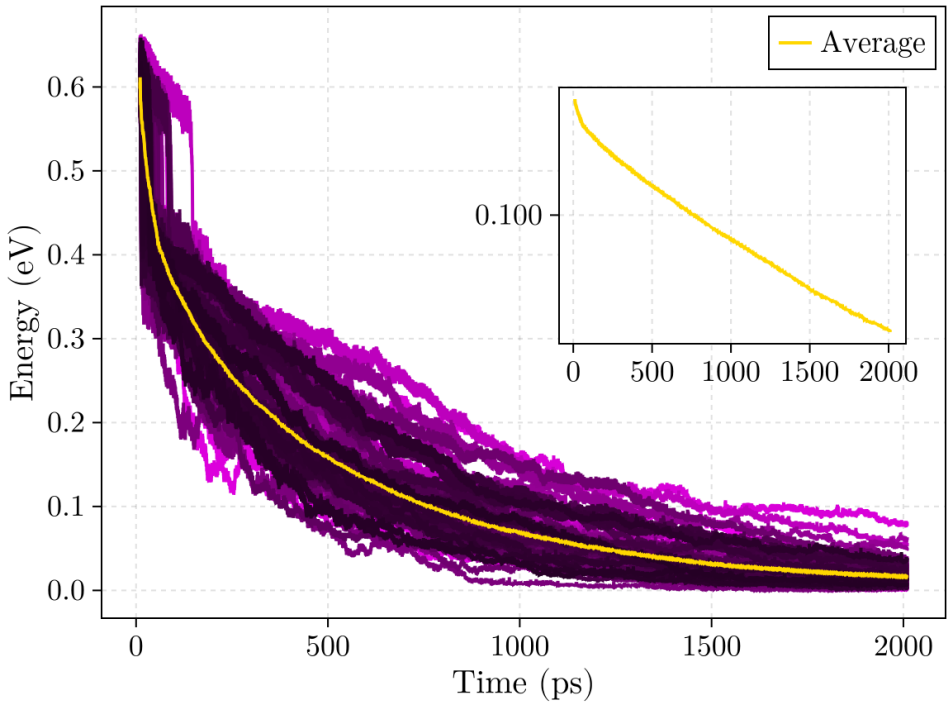

Figure 6.11: Same as Figure 6.3 but using the site-site potential for the CO-am ^{13}CO case with a 0.6 eV excitation energy.

mechanical description provided by Corcelli and Tully [19] for a CO film adsorbed on NaCl(100).

6.7 Summary and Outlook

We performed classical NEMD simulations of the VER of combinations of four different CO isotopologues, in both amorphous and crystalline clusters. Using trajectory ensembles we have determined average VER lifetimes in the order of nanoseconds from these simulations.

Originally motivated by the frequency-gap law, we have developed a novel analysis technique which allows to analyze the frequency-gap dependence $\Delta\nu$ of the decay time constants τ. An offset between decay time constants at positive and negative frequency-gaps was observed, where the VER rate was faster when the excited frequency was lower than the accepting frequency. These negative frequency-gaps are

only possible when the excited molecule is a different isotopes from the cluster, hence, we attribute this offset to a difference in anharmonic coupling between molecules of the same isotope and those of different isotopes. Crystalline clusters exhibit a different frequency-gap dependence than that of the amorphous clusters, where the VER was most efficient near $|\Delta\nu| = 50$ cm^{-1}.

A detailed analysis of the energy redistribution has revealed that vibrational energy dissipated into the cluster predominantly excites vibrational stretch modes of the surrounding molecules. This is not surprising when comparing to collisions of pairs of vibrationally excited CO molecules in gas phase: Chen *et al.*[29] found a lack of energy conversion between vibrational and rotational or translational energy. They attributed the lack of energy conversion to the energy-gap law, owing to the fact that vibrational quanta are much higher in energy than their rotational counterparts or the continuum provided by translational motion. The fact that rotational and translational modes form the low-frequency parts of the VDOS of the different forms of solid carbon monoxide studied here does not change the validity of this argument. Experiments for a monolayer of CO adsorbed on an NaCl(100) surface convey the same trend. Chang and Ewing[49] measured the rate of vibrationally induced desorption and found that is a slow process for this system due to inefficient energy transfer from vibrational to rotational and translation degrees of freedom.

Although the energy transfer occurs continuously in our classical simulations, further analysis of our trajectory ensembles elucidates very interesting analogies to the quantum mechanical description of V–V energy transfer for CO adsorbed on an NaCl(100) established by Corcelli and Tully[19]. While their model assumes parallel CO molecules that couple only through dipole-dipole interactions only, our cluster studies include more variation in the angular distribution (amorphous clusters in particular), and the interactions between CO molecules are not limited to dipole-dipole interactions. Apart from that, our novel analysis technique has allowed us to identify a qualitative change of the $\tau(\Delta\nu)$ relation when $\Delta\nu$ reaches the tail of the low-frequency VDOS – analogous to what the quantum mechanical theory predicts when switching from one-phonon to two phonon-assisted non-resonant V–V energy transfer. From the time evolution of the vibrational energy alone it is not easily noticed that this occurs, thus highlighting the usefulness of our novel technique. Furthermore, when the frequency-gap was essentially zero, we have observed a classical manifestation of the resonant V–V energy transfer mechanism described by Corcelli and Tully[19]. We found this mechanism to be independent of the cluster structure, indicating no strict dependence on orientation or LVM–LVM coupling. For the crystalline clusters, the

$\tau(\Delta\nu)$ analysis suggests that the VDOS influences the non-resonant V–V transfer in a different way than for the amorphous clusters, which requires more work to enable better understanding in the future.

Both non-resonant and resonant V–V energy transfer together with the absence of pronounced multi-phonon-assisted direct dissipation to low-frequency modes are the crucial ingredients for the vibrational energy pooling that has been observed for CO adsorbed on an NaCl(100). Considering that all of these ingredients seem to be captured by our classical simulations, future work with our computational setup could help to better understand if and if so how vibrational energy pooling could also occur in solid CO structures.

6.8 Data Availability Statement

All of the Julia code used for the simulations is publicly available on GitHub at https://github.com/Cavenfish/JMD. An HDF5 compliant dataset (Julia Data Format ".jld2") of all ensemble averages reported within the manuscript can be found on Zenodo at https://zenodo.org/records/14237514.

6.A Appendix

6.A.1 Size Convergence Tests

Since we do not employ periodic boundary conditions, we verified that the cluster size was large enough to capture all long-range interaction influencing the VER. Figure 6.A.12 shows the ensemble average energy decay for three different cluster sizes (100, 250 and 500 molecules), along with the cluster temperature below it.

There is very little difference between the three sizes, in agreement with VER theory which predicts a large radial decay for the vibrational energy transfer efficiency. Although there is little change in the VER lifetimes, the cluster temperature gain is largely affected by the size. Despite the temperature reported increasing due to excitation, the energy remains nearly entirely in vibrational energy which does not result in evaporation of the cluster. We opted to use clusters of 250 molecules since it provided an ideal compromise between temperature stability and computational efficiency.

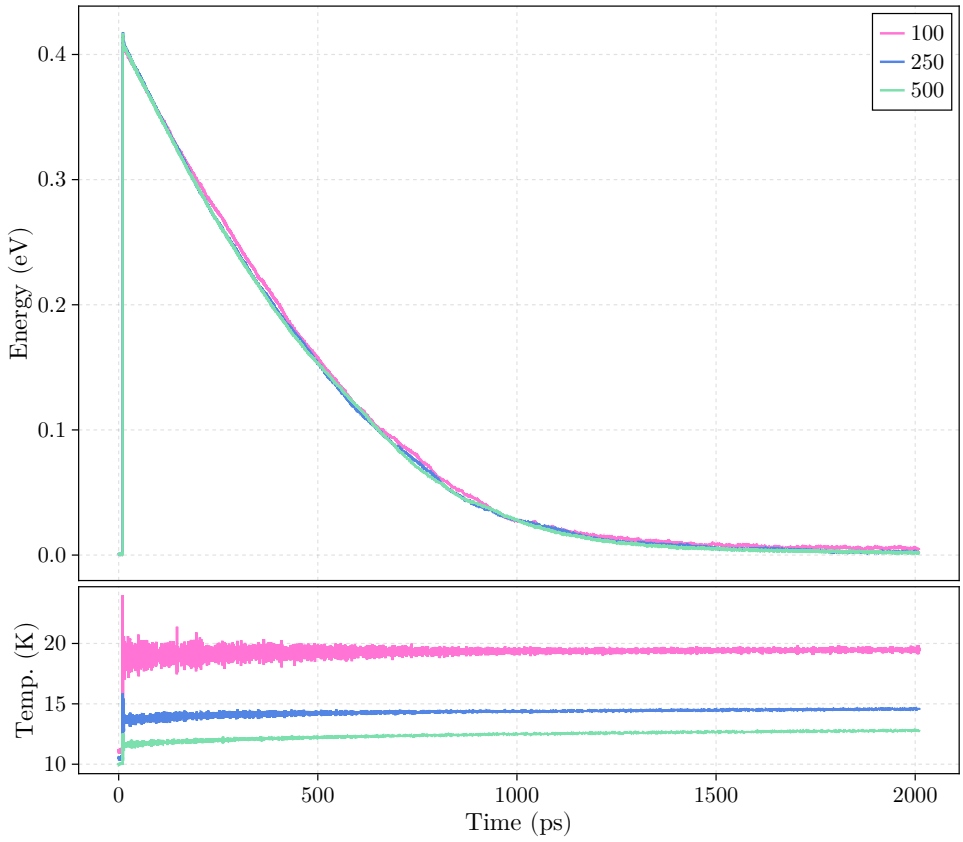

Figure 6.A.12: Upper panel: ensemble average of the vibrational energy of an excited CO molecule within an amorphous CO cluster. Lower panel: the cluster temperature during VER simulation. In both cases the 10 ps equilibration NVE simulation is included to illustrate the gain in temperature during excitation.

6.A.2 Geometric and Vibrational Properties for the PIP–NN Potential

Figure 6.A.13 compares the radial distribution (top left), angular distribution (top right) and the number of participating molecules per vibrational mode (bottom) of crystalline and amorphous CO using the PIP–NN potential.

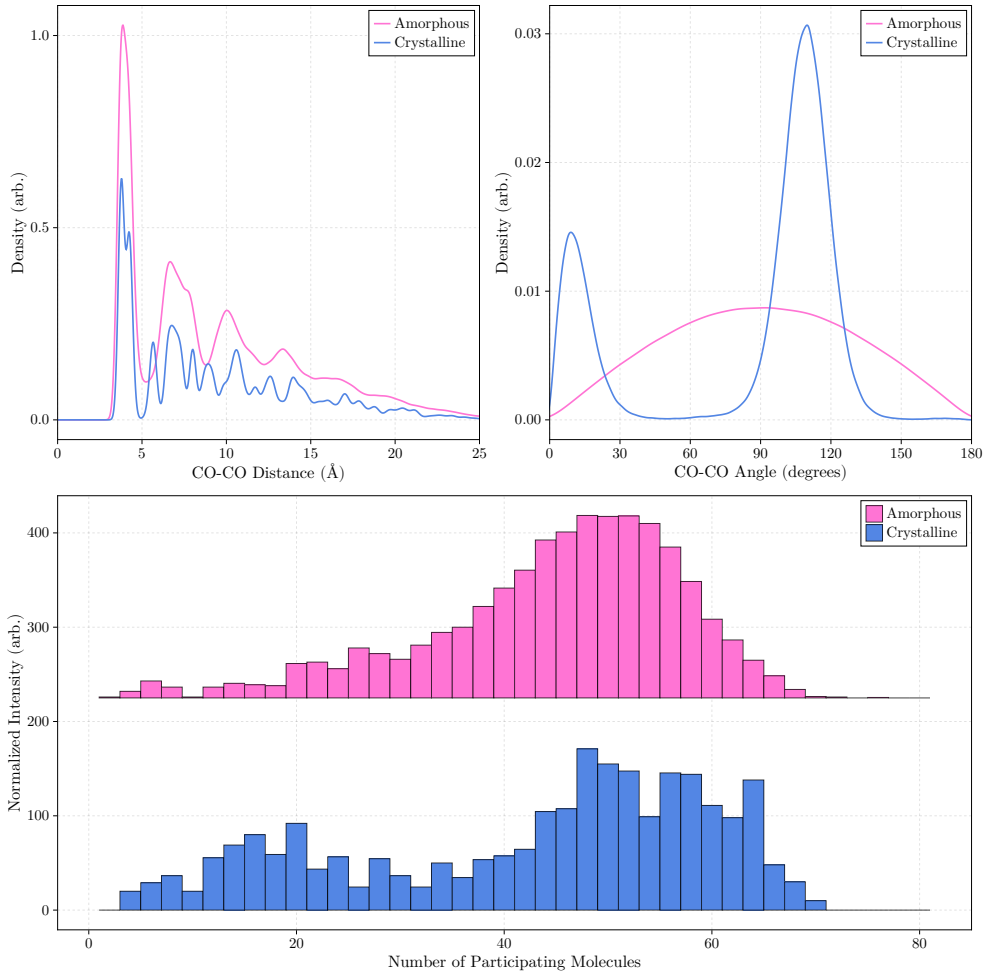

Figure 6.A.13: Same as Figure 1 in the main article but using the PIP–NN potential instead of the site–site potential.

6.A.3 Decomposition of Phonon DOS

Figure 6.A.14 shows the decomposition of the phonon DOS into surface and bulk contributions using the site–site potential.

Figure 6.A.15 shows the decomposition of the phonon DOS into surface and bulk contributions using the PIP–NN potential.

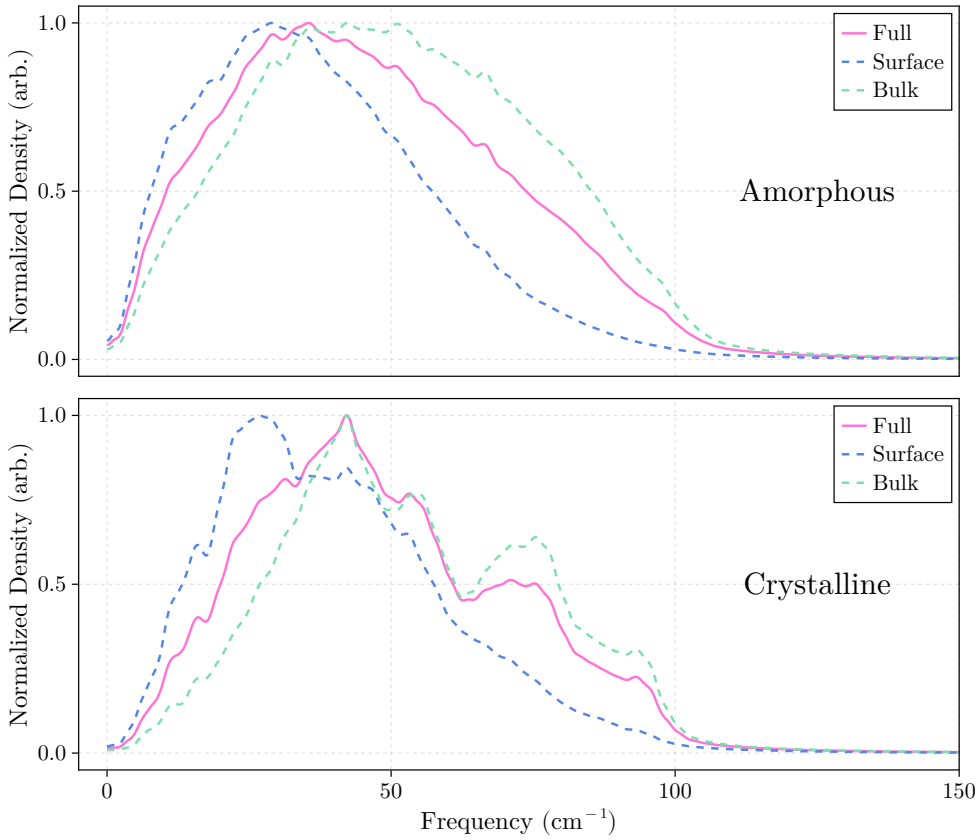

Figure 6.A.14: Decomposition of the phonon DOS shown in the upper panel of Figure 2 in the main article (using the site–site potential).

6.A.4 Trajectory Ensemble for Crystalline Clusters

Figure 6.A.16 shows the total energy of the excited molecule versus time (purple lines) for all simulaitons, and the average (gold) using the site–site potential for crystalline clusters.

6.A.5 Decomposition of Bi-Exponential Fits for Non-Resonant Energy Transfer

Figure 6.A.17 show the decomposition of the bi-exponential fit to the data shown in the top left panel of Figure 10.

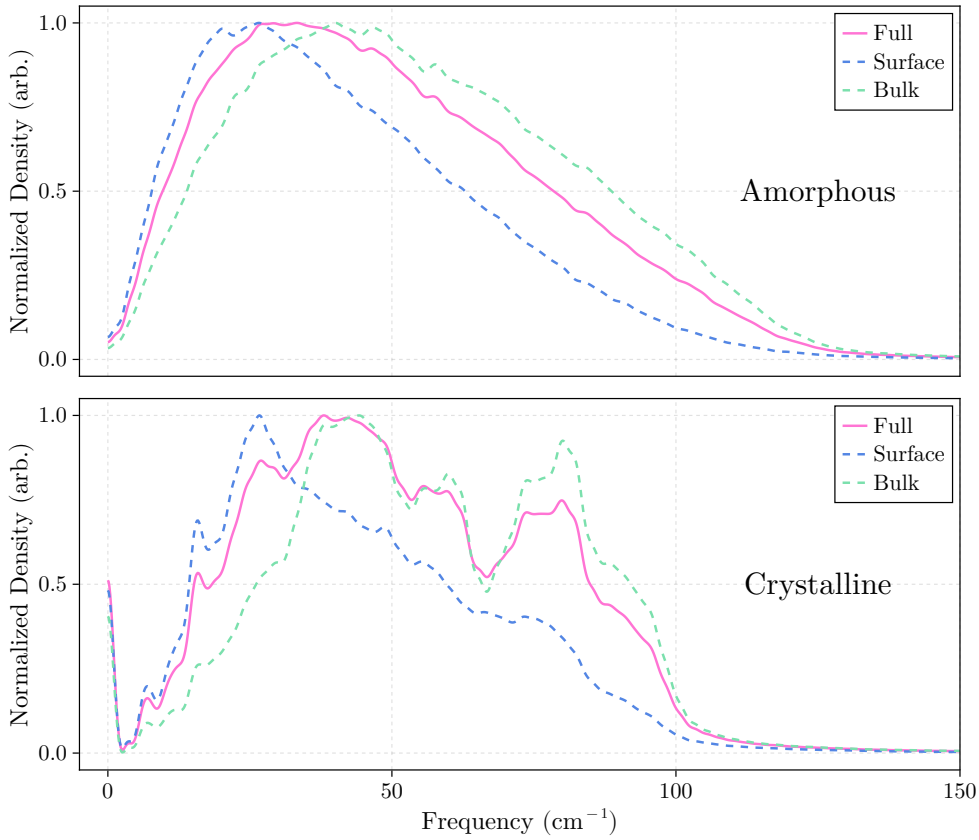

Figure 6.A.15: Decomposition of the phonon DOS shown in the lower panel of Figure 2 in the main article (using the PIP–NN potential).

Figure 6.A.18 show the decomposition of the bi-exponential fit to the data shown in the top right panel of Figure 10.

Figure 6.A.19 show the decomposition of the bi-exponential fit to the data shown in the bottom left panel of Figure 10.

Figure 6.A.20 show the decomposition of the bi-exponential fit to the data shown in the bottom right panel of Figure 10.

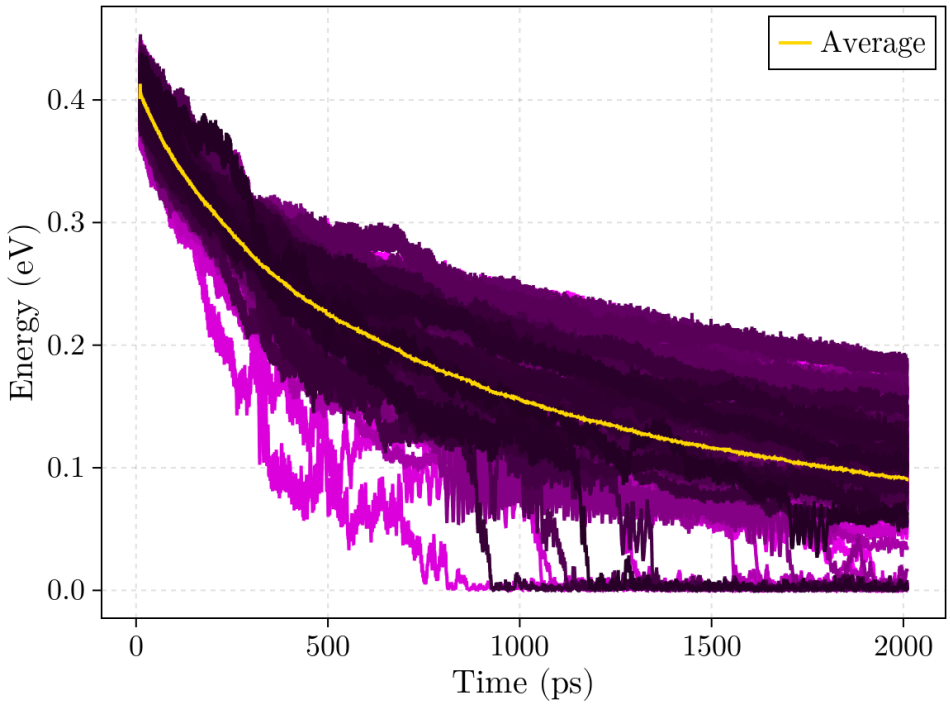

Figure 6.A.16: Same as Figure 3 in in the main article but for crystalline clusters.

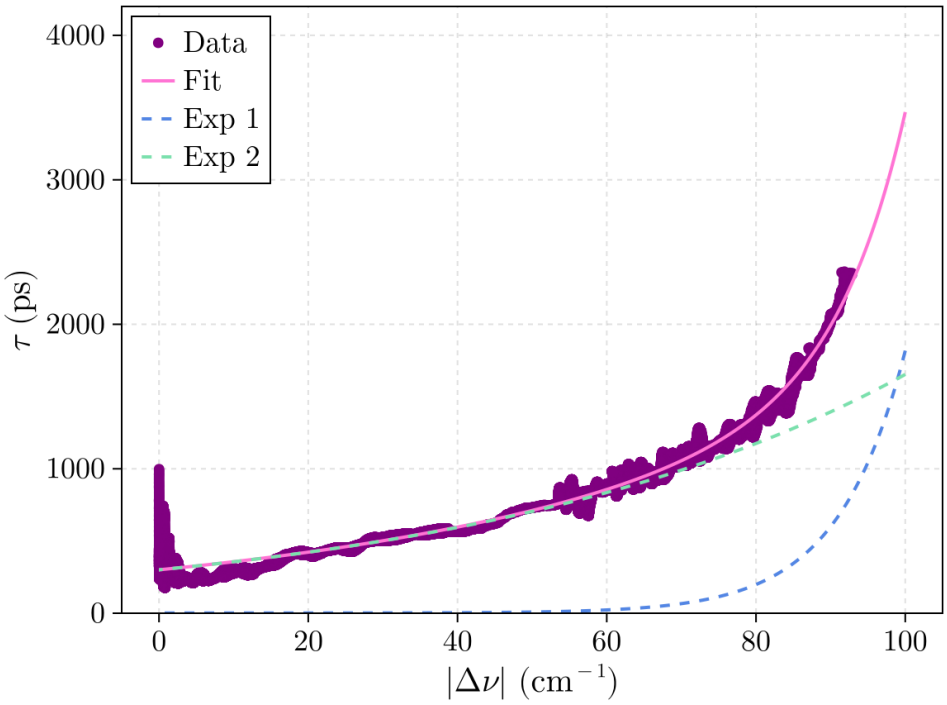

Figure 6.A.17: Decomposition of the bi-exponential fit to the τ data shown in the top left panel of Figure 10. Note that $|\Delta\nu|$ is plotted here and in the subsequent figures to enable a better comparison of the exponential fits.

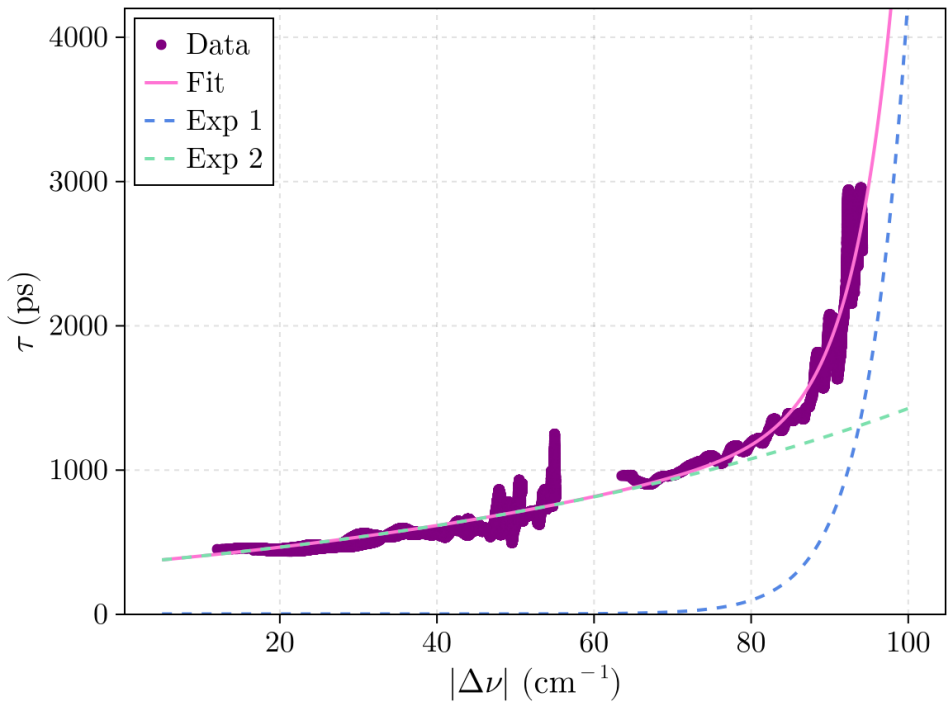

Figure 6.A.18: Same as Figure 6.A.17 but for the top right panel of Figure 10.

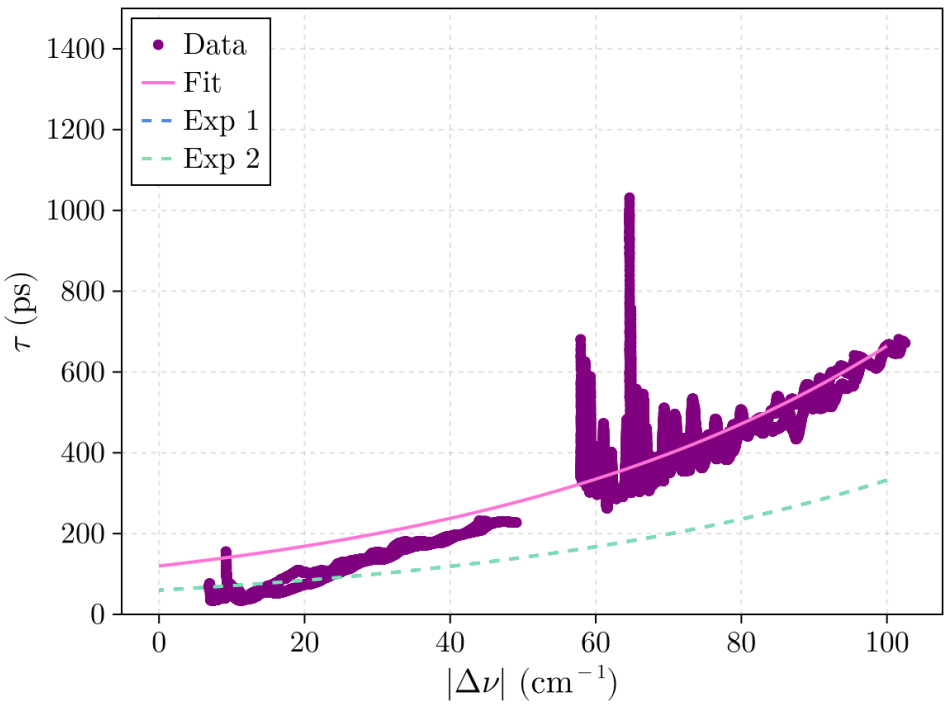

Figure 6.A.19: Same as Figure 6.A.17 but for the bottom left panel of Figure 10.

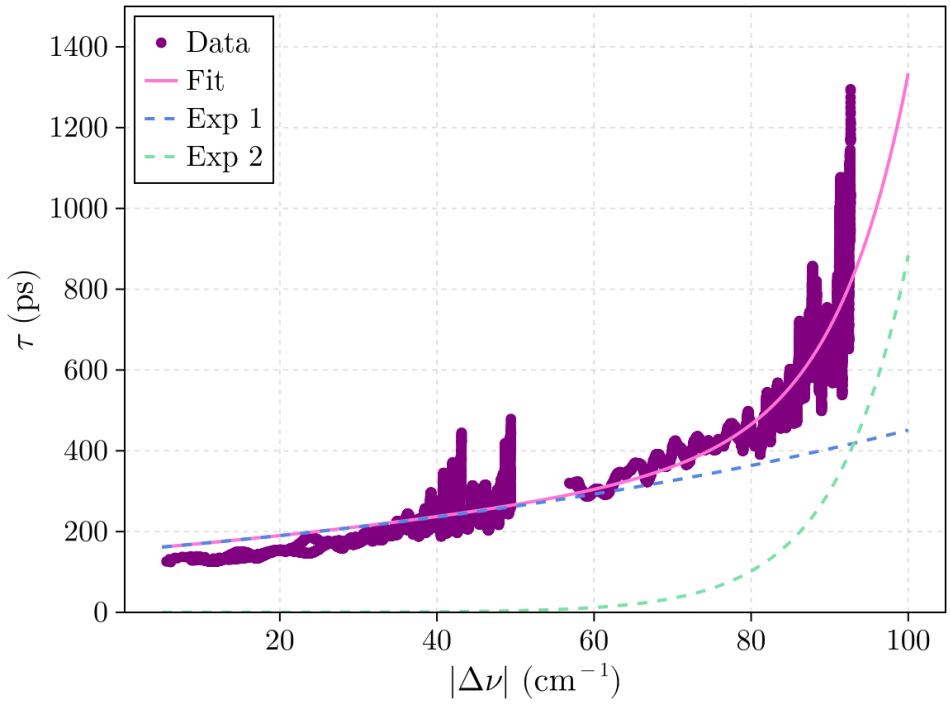

Figure 6.A.20: Same as Figure 6.A.17 but for the bottom right panel of Figure 10.

6.B Bibliography

[1] JC Owrutsky, D Raftery, and RM Hochstrasser. Vibrational relaxation dynamics in solutions. *Annual Review of Physical Chemistry*, 45(1):519–555, 1994.

[2] David R Glowacki, CH Liang, Stephen P Marsden, Jeremy N Harvey, and Michael J Pilling. Alkene hydroboration: hot intermediates that react while they are cooling. *Journal of the American Chemical Society*, 132(39):13621–13623, 2010.

[3] Barry K Carpenter, Jeremy N Harvey, and Andrew J Orr-Ewing. The study of reactive intermediates in condensed phases. *Journal of the American Chemical Society*, 138(14):4695–4705, 2016.

[4] Hiroshi Fujisaki and John E Straub. Vibrational energy relaxation in proteins. *Proceedings of the National Academy of Sciences*, 102(19):6726–6731, 2005.

[5] David M Leitner. Energy flow in proteins. *Annual Review of Physical Chemistry*, 59(1):233–259, 2008.

[6] Martin Gruebele and Peter Guy Wolynes. Vibrational energy flow and chemical reactions. *Accounts of Chemical Research*, 37(4):261–267, 2004.

[7] Qizhen Hong, Loriano Storchi, Quanhua Sun, Massimiliano Bartolomei, Fernando Pirani, and Cecilia Coletti. Improved quantum–classical treatment of n2–n2 inelastic collisions: Effect of the potentials and complete rate coefficient data sets. *Journal of Chemical Theory and Computation*, 19(23):8557–8571, 2023.

[8] Qizhen Hong, Loriano Storchi, Cecilia Coletti, Jia Li, Quanhua Sun, and Jun Li. Quantum-classical rate coefficient datasets of vibrational energy transfer in carbon monoxide based on highly accurate potential energy surface. *The Journal of Chemical Physics*, 160(8), 2024.

[9] Zhen Zhang, Lukasz Piatkowski, Huib J Bakker, and Mischa Bonn. Ultrafast vibrational energy transfer at the water/air interface revealed by two-dimensional surface vibrational spectroscopy. *Nature Chemistry*, 3(11):888–893, 2011.

[10] Prerna Sudera, Jenée D Cyran, Malte Deiseroth, Ellen HG Backus, and Mischa Bonn. Interfacial vibrational dynamics of ice ih and liquid water. *Journal of the American Chemical Society*, 142(28):12005–12009, 2020.

[11] Robert Englman and Joshua Jortner. The energy gap law for radiationless transitions in large molecules. *Molecular Physics*, 18(2):145–164, 1970.

[12] Abraham Nitzan, Shaul Mukamel, and Joshua Jortner. Energy gap law for vibrational relaxation of a molecule in a dense medium. *The Journal of Chemical Physics*, 63(1):200–207, 1975.

[13] Baozhou Sun, GA Shi, SVS Nageswara Rao, Michael Stavola, NH Tolk, SK Dixit, LC Feldman, and G Lüpke. Vibrational lifetimes and frequency-gap law of hydrogen bending modes in semiconductors. *Physical Review Letters*, 96(3):035501, 2006.

[14] Alexander Kandratsenka, Jörg Schroeder, Dirk Schwarzer, and Vyacheslav S Vikhrenko. Nonequilibrium molecular dynamics simulations of vibrational energy relaxation of hod in D_2O. *The Journal of Chemical Physics*, 130(17), 2009.

[15] G Lüpke, X Zhang, Baozhou Sun, A Fraser, NH Tolk, and LC Feldman. Structure-dependent vibrational lifetimes of hydrogen in silicon. *Physical Review Letters*, 88(13):135501, 2002.

[16] D West and SK Estreicher. Isotope dependence of the vibrational lifetimes of light impurities in si from first principles. *Physical Review B*, 75(7):075206, 2007.

[17] KK Kohli, Gordon Davies, NQ Vinh, D West, SK Estreicher, I Izeddin, and KM Itoh. Isotope dependence of the lifetime of the 1136-cm-1 vibration of oxygen in silicon. *Physical Review Letters*, 96(22):225503, 2006.

[18] Huan-Cheng Chang and George E Ewing. Infrared fluorescence from a monolayer of co on nacl (100). *Physical Review Letters*, 65(17):2125, 1990.

[19] SA Corcelli and JC Tully. Vibrational energy pooling in co on nacl (100): Methods. *The Journal of Chemical Physics*, 116(18):8079–8092, 2002.

[20] Li Chen, Jascha A Lau, Dirk Schwarzer, Jörg Meyer, Varun B Verma, and Alec M Wodtke. The sommerfeld ground-wave limit for a molecule adsorbed at a surface. *Science*, 363(6423):158–161, 2019.

[21] SA Corcelli and JC Tully. Vibrational energy pooling in co on nacl (100): Simulation and isotope effects. *The Journal of Physical Chemistry A*, 106(45):10849–10860, 2002.

[22] Jeff Bezanson, Alan Edelman, Stefan Karpinski, and Viral B Shah. Julia: A fresh approach to numerical computing. *SIAM Review*, 59(1):65–98, 2017.

[23] P Mogensen and A Riseth. Optim: A mathematical optimization package for julia. *Journal of Open Source Software*, 3(24):615, 2018.

[24] Christopher Rackauckas and Qing Nie. Differentialequations.jl–a performant and feature-rich ecosystem for solving differential equations in julia. *Journal of Open Research Software*, 5(1):151, 2017.

[25] Simon Danisch and Julius Krumbiegel. Makie.jl: Flexible high-performance data visualization for julia. *Journal of Open Source Software*, 6(65):3349, 2021.

[26] Matteo Frigo and Steven G Johnson. Fftw: An adaptive software architecture for the fft. In *Proceedings of the 1998 IEEE International Conference on Acoustics, Speech and Signal Processing, ICASSP'98 (Cat. No. 98CH36181)*, volume 3, pages 1381–1384. IEEE, 1998.

[27] C Bradford Barber, David P Dobkin, and Hannu Huhdanpaa. The quickhull algorithm for convex hulls. *ACM Transactions on Mathematical Software (TOMS)*, 22(4):469–483, 1996.

[28] Marc C van Hemert, Junko Takahashi, and Ewine F van Dishoeck. Molecular dynamics study of the photodesorption of co ice. *The Journal of Physical Chemistry A*, 119(24):6354–6369, 2015.

[29] Jun Chen, Jun Li, Joel M Bowman, and Hua Guo. Energy transfer between vibrationally excited carbon monoxide based on a highly accurate six-dimensional potential energy surface. *The Journal of Chemical Physics*, 153(5):054310, 2020.

[30] Brian C. Ferrari, Germán Molpeceres, Johannes Kästner, Yuri Aikawa, Marc van Hemert, Jörg Meyer, and Thanja Lamberts. Floating in space: How to treat the weak interaction between co molecules in interstellar ices. *ACS Earth and Space Chemistry*, 7(7):1423–1432, 2023. doi: 10.1021/acsearthspacechem.3c00086.

[31] Samuel Del Fré, Alejandro Rivero Santamaría, Denis Duflot, Romain Basalgète, Géraldine Féraud, Mathieu Bertin, Jean-Hugues Fillion, and Maurice Monnerville. Mechanism of ultraviolet-induced co desorption from co ice: Role of vibrational relaxation highlighted. *Physical Review Letters*, 131(23):238001, 2023.

[32] Giovanni Bussi, Davide Donadio, and Michele Parrinello. Canonical sampling through velocity rescaling. *The Journal of Chemical Physics*, 126(1):014101, 2007.

[33] Loup Verlet. Computer “experiments" on classical fluids. i. thermodynamical properties of lennard-jones molecules. *Physical Review*, 159(1):98, 1967.

[34] William C Swope, Hans C Andersen, Peter H Berens, and Kent R Wilson. A computer simulation method for the calculation of equilibrium constants for the formation of physical clusters of molecules: Application to small water clusters. *The Journal of Chemical Physics*, 76(1):637–649, 1982.

[35] Barbara Okray Hall and Hubert M James. Lattice dynamics of α carbon monoxide. *Physical Review B*, 13(8):3590, 1976.

[36] Yanqiang Han, Jinyun Liu, and Jinjin Li. Ab initio investigation of solid carbon monoxide phase diagram at low temperature. *Materials Today Communications*, 28:102571, 2021.

[37] MC Van Hemert. Potential energy surface for the study of inelastic collisions between nonrigid co and h_2. *The Journal of Chemical Physics*, 78(5):2345–2354, 1983.

[38] Franco A Gianturco. *The transfer of molecular energies by collision: recent quantum treatments*, volume 11. Springer Science & Business Media, 2012.

[39] Peter Kahlig. Some aspects of julius von hann's contribution to modern climatology. *Interactions Between Global Climate Subsystems: The Legacy of Hann*, 75: 1–7, 1993.

[40] G Guelachvili. Absolute wavenumbers and molecular constants of the fundamental bands of $^{12}c^{16}o$, $^{12}c^{17}o$, $^{12}c^{18}o$, $^{13}c^{16}o$, $^{13}c^{17}o$, $^{13}c^{18}o$ and of the 2-1 bands of $^{12}c^{16}o$ and $^{13}c^{16}o$, around 5μm, by fourier spectroscopy under vacuum. *Journal of Molecular Spectroscopy*, 75(2):251–269, 1979.

[41] LJ Karssemeijer, S Ioppolo, MC Van Hemert, A Van Der Avoird, MA Allodi, GA Blake, and HM Cuppen. Dynamics of co in amorphous water-ice environments. *The Astrophysical Journal*, 781(1):16, 2013.

[42] BM Giuliano, AA Gavdush, B Müller, KI Zaytsev, T Grassi, AV Ivlev, Maria Elisabetta Palumbo, GA Baratta, C Scire, GA Komandin, *et al.* Broadband spectroscopy of astrophysical ice analogues-i. direct measurement of the complex re-

fractive index of co ice using terahertz time-domain spectroscopy. *Astronomy & Astrophysics*, 629:A112, 2019.

[43] Wei Lee and Thomas J Wdowiak. Laboratory fourier-transform terahertz spectroscopy for molecular ices of astrophysical interest: Solid co as an example. *Japanese Journal of Applied Physics*, 43(10R):7303, 2004.

[44] NB Slater. Classical motion under a morse potential. *Nature*, 180(4598):1352–1353, 1957.

[45] Robert F Goldstein and William Bialek. Vibronically coupled two-level systems: Radiationless transitions in the slow regime. *Physical Review B*, 27(12):7431, 1983.

[46] Xiaoyong Zhang, Saulo A Vazquez, and Jeremy N Harvey. Vibrational energy relaxation of deuterium fluoride in d-dichloromethane: insights from different potentials. *Journal of Chemical Theory and Computation*, 17(3):1277–1289, 2021.

[47] Abraham Savitzky and Marcel JE Golay. Smoothing and differentiation of data by simplified least squares procedures. *Analytical Chemistry*, 36(8):1627–1639, 1964.

[48] Jascha A Lau, Li Chen, Arnab Choudhury, Dirk Schwarzer, Varun B Verma, and Alec M Wodtke. Transporting and concentrating vibrational energy to promote isomerization. *Nature*, 589(7842):391–395, 2021.

[49] Huan-Cheng Chang and George E Ewing. The quantum efficiency of vibrationally induced desorption for a monolayer of co on nacl (100). *Chemical Physics*, 139 (1):55–65, 1989.

.0 Bibliography